

该文档是极速PDF编辑器生成，
如果想去掉该提示，请访问并下载：
<http://www.jisupdfeditor.com/>



The two typical excitatory cell types granule cell (GCs) and mossy cells of DG (dentate gyrus) see fig 1 in chronically epileptic mice identified by optogenetic tagging are studied through the electrographic data of the seizure. For both GC and MC, the reconfiguration are tested related to spatial representations via the emergence, extinction and rate alteration of firing fields. To investigate the consequences of MC and GC loss on cognition, the activities of the cell neurons are recorded by MEA/EEG/MEG. Further, gene expression (fig:2) and protein analysis is applied to understand the functionality of them in addition to the intrinsic level. One machine learning method based on Bayes Variational Inference model is applied to the t-SNE[1] clustering of the genes. As DNA and RNA are usually of high dimension, the Bayes variance is utilised to modify the BIC in guaranteeing the convergence, computing KL and perplex and the cluster distance are measured with Euclid metric simulating with normal and gamma distribution. In the MEA analysis, another machine learning method combining Hamilton Markov chain likelihood-free model[2, 3] is applied on ictal classifications as well as different auto-correlation, gaps, asymmetry, amplitude, phase angle and etc. on different time windows and bands. In the genetic analysis, more analysis with the expression is on regenerated data according to its distribution. One review comparing epilepsy with AD in genetic regulation is introduced as well for giving guide on epilepsy gene detection method as well. More prominent work see the references[12].

$$q_{i,j} = \frac{(1 + |y_i - y_j|^2)^{-1}}{\sum (1 + |y_s - y_t|^2)^{-1}}$$
$$p_{i,j} = (p_{i|j} + p_{j|i})/2n$$
$$p_{i|j} = \frac{\exp(-|x_i - x_j|^2 / 2\sigma_j^2)}{\sum \exp(-|x_s - x_t|^2 / 2\sigma_j^2)}$$
$$KL(P \parallel Q) = \sum p_{i,j} * \log \frac{p_{i,j}}{q_{i,j}}$$
$$Perplex(p_j) = 2^{H(p_j)}, \text{ where } H(P_j) = -\sigma_j p_{i|j} * \log_2 p_{i|j}$$
$$Perplex(p_i) = Perplex$$

, where Perplex is the hyperparameter of the t-SNE central to the final cluster.

Large Perplex usually leads to the embedding sub-optimal in detecting the pattern of the data(In the limit, when the Perplex goes to the number of data points, the corresponding embedding form a Gaussian or uniform like distribution and fails to be useful for structure detection at all) and thus, we design a new criteria:

$$BIC = -2 * \log(L) + \log(n) * k$$

, where the first term stands for the goodness-of-fit of the maximum-likelihood-estimation and the second controls the complexity of the model with penalty k scaled by $\log(n)$.

Intuitively, when Perplex increases, differences among points will become less and less significant with regard to the length of the kernel in distribution P, and P will tend to uniform. The forward form of KL has large cost for under-estimating probability but not for over-estimating. That is, if $p_{i,j}$ is large and $q_{i,j}$ is small, KL divergence is large while in the opposite direction, KL is not affected. Increasing Perplex leads to larger σ_j and more uniform $p_{i,j}$ so it is easier for the student-t distribution in low dimensional space to assign mass for all probability points sufficiently. This is the so called crowding problem: When projecting from high to low dimensional space, there is not enough room in lower dimensional space. Generally, increasing Perplex relaxes the problem and reduces the amount of structure to be modelled with less error according to KL while pays a cost in the second term. With the practical test, we apply it on the MC GC cell expression classification (fig 3 - 5) with t-SNE.

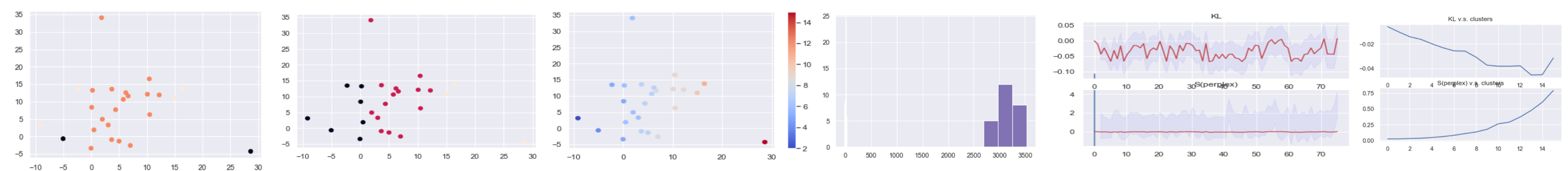
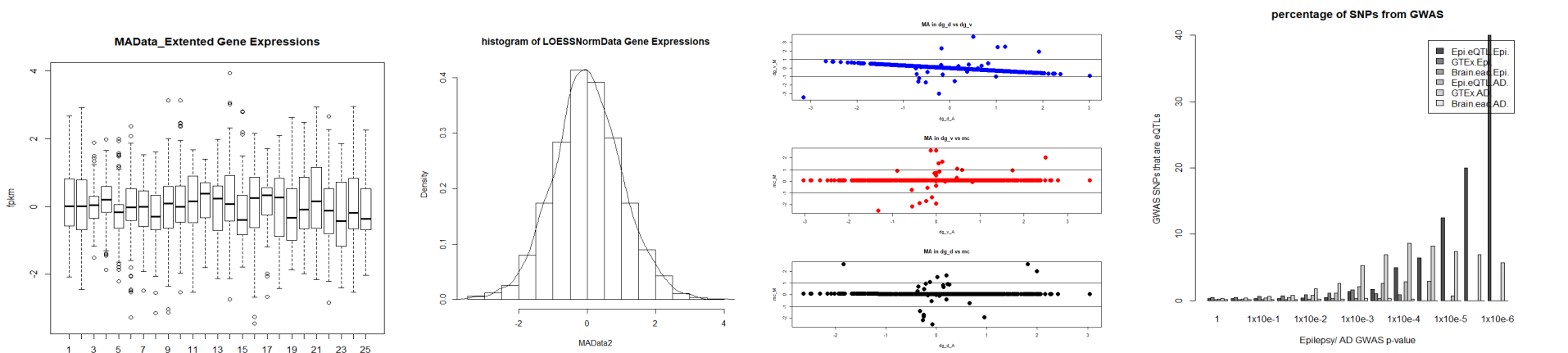


Figure 1: A 3x3 grid of plots showing the effect of different base models on the performance of the proposed model. The rows represent different base models: 'No base model', 'Auto base model', and 'ML base model'. The columns represent different target models: 'No target model', 'ML target model', and 'Auto target model'. Each plot shows the 'Performance' (Y-axis, 0.0 to 1.0) versus 'Number of iterations' (X-axis, 0 to 100). The plots show that the proposed model (blue line) generally outperforms the baseline (red line) across all configurations. The 'Auto base model' and 'ML base model' configurations show higher performance than the 'No base model' configuration. The 'Auto target model' configuration shows the highest performance, reaching a plateau around 0.9. The 'ML target model' configuration shows a performance around 0.7. The 'No target model' configuration shows the lowest performance, around 0.5. The 'Auto base model' and 'ML base model' configurations show a slight decrease in performance as the number of iterations increases, while the 'No base model' configuration shows a slight increase. The 'Auto target model' configuration shows a slight decrease in performance as the number of iterations increases, while the 'ML target model' and 'No target model' configurations show a slight increase.

As study of cellular processes existing inside intact organisms requires methods to visualize cellular functions such as gene expression in deep tissues, the 75 regenerated expression dataset (seen in fig 13, dg-d, dg-v and MC cell separately) is studied along with the gene regulation as the substrate of the observable trait at which the genotype gives rise to the phenotype (further cellular differentiation adaptability of organism in the versatility and adaptability). After the LOESS normalization, it is normalized according to QC test (fig:14) and most genes of mc and dg-d are expressed stationarily with MA value (fig:15) mainly distributed around zero (since the expression of genes are assumed to be unchanged at certain tissue region.) while has decreasing trend for the dg-v expression. (More in log2 expression and MDR plot can be found in ref [12], including one review about epilepsy and AD comparison study through eQTL, fig: 16.)


$$\begin{aligned} \lambda &\leftarrow (\log \hat{r}(\mathbf{x} | \boldsymbol{\theta}_k) + \log p(\boldsymbol{\theta}_k)) - (\log \hat{r}(\mathbf{x} | \boldsymbol{\theta}_t) + \log p(\boldsymbol{\theta}_t)) + K(\mathbf{m}_k) - K(\mathbf{m}_t) \\ \rho &\leftarrow \min(\exp(\lambda), 1) \end{aligned} \quad \boldsymbol{\theta}_{t+1} \leftarrow \begin{cases} \boldsymbol{\theta}_k & \text{with probability } \rho \\ \boldsymbol{\theta}_t & \text{with probability } 1 - \rho \end{cases}$$

$$\begin{aligned} \lambda &\leftarrow (\log \hat{r}(\mathbf{x} | \boldsymbol{\theta}_k) + \log p(\boldsymbol{\theta}_k)) - (\log \hat{r}(\mathbf{x} | \boldsymbol{\theta}_t) + \log p(\boldsymbol{\theta}_t)) + K(\mathbf{m}_k) - K(\mathbf{m}_t) \\ \rho &\leftarrow \min(\exp(\lambda), 1) \end{aligned} \quad \boldsymbol{\theta}_{t+1} \leftarrow \begin{cases} \boldsymbol{\theta}_k & \text{with probability } \rho \\ \boldsymbol{\theta}_t & \text{with probability } 1 - \rho \end{cases}$$

Bayes inference model[5,15] combined with Hamilton Markov(fig: 17)[2] sampling is utilized as the updating of dynamic information of the MEA signal, with the prior knowledge of the different ictal patterns decomposed by empirical mode decomposition(EMD) with intrinsic mode functions(IMF), after computing the entropy, instantaneous energy and frequencies, it is classified[14] based on likelihood-free method. To further study the ictal/interictal, HFO parts are extracted with filter threshold as 80Hz(ripples) and 250Hz(fast ripples) separately and with more than 9 spikes detected in bins of duration at least 10ms.

Result of linear regression with accuracy: 0.0

Parameter	Value	Unit	Min	Max
Learning rate	0.001		0.000	0.001
Batch size	32		32	32
Number of epochs	10000		10000	10000
Number of hidden units	10		10	10
Number of output units	10		10	10
Number of input units	10		10	10
Number of hidden layers	1		1	1
Number of output layers	1		1	1
Number of input layers	1		1	1
Number of hidden units per layer	10		10	10
Number of output units per layer	10		10	10
Number of input units per layer	10		10	10

Result of linear regression with accuracy: 0.8

Parameter	Value	Unit	Min	Max
Learning rate	0.001		0.000	0.001
Batch size	32		32	32
Number of epochs	10000		10000	10000
Number of hidden units	10		10	10
Number of output units	10		10	10
Number of input units	10		10	10
Number of hidden layers	1		1	1
Number of output layers	1		1	1
Number of input layers	1		1	1
Number of hidden units per layer	10		10	10
Number of output units per layer	10		10	10
Number of input units per layer	10		10	10

In summary, according to the correlation is latest within one window on delta band and gamma band (with the maximum around 90 ms. The histogram and the gap can be seen distributed with gamma and normal distribution. According to the filtered signal, the type of the spike is classified as 'broad, broad, broad, narrow, broad, narrow, broad, broad, broad, broad' with (fig 18)linear regression model($\text{acc}=0.9$ fig: 19): T type asymmetry+duration+Asymmetry/distance+Q3Distance(gap)+Q3Distance/sigma and finally into 'interictal, ictal, ictal, interictal, interictal' after (fig: 20)JMF($\text{acc}=0.8$ in fig: 21). Detailed sensitivity, specificity, precision, misrate and false discovery and other evaluations along with ANOVA tests can be found in [12] (bin 80 see fig 22)

With the normalized expression data ($p = 0.0035$ with ks-test), Genes expressed in the 3-sigma distance, Cdc45, Prox1, Stt18, Marskl1, SOX2, Cdk4 and etc. known to have distinct functions are shown in the heatmap and accordingly possess correlation with close to zero in the correlation figure. However, to explore the difference of the function on cellular scale, the Welch two-sampled t-test is applied. According to the result, the gene expression for dg-d, dg-v and mc ($p = 0.009724$, $p = 0.008046$ and $p = 0.008584$) are not of the same mean on \log_2 level. Generally, dg-d and mc are expressed more evenly while dg-v is distributed on some specific dimension (correction method will be applied in the next step exploration.) To explore the transcription of DNA in the future, we also introduced one review of genetic regulation of gene expression in human hippocampus [13].

[1] G. E. van der Maaten, L. J. P.; Hinton. <i>Visualizing Data Using t-SNE</i> . Journal of Machine Learning Research, 2008.	[10] S Kullback. <i>Information Theory and Statistics</i> . John Wiley Sons, 1978.
[2] Louppe/University of Liège Joeri Hermans, Volodimir Begy Gilles. <i>Likelihood-free MCMC with Amortized Approximate Likelihood Ratios</i> .	[11] On the Importance of Strong Baselines in Bayesian Deep Learning.
[3] Annikla Ahlmanen Qn He, Jari Hyttinen. <i>Classification of epileptic ictal with Bayes inference Model</i> . Neuroelectronic Interfaces (GRS) Gordon Research Seminars, 2019.	[12] RNA single sequences report.
[4] Dentate granule and mossy cells exhibit distinct spatiotemporal responses to local change in a one-dimensional landscape of visual cortex cues.	[13] Genetic regulation of gene expression in the epileptic human hippocampus.
[5] Lévesque. <i>Robustness Quantities for Bayesian Inference with Gaussian Processes</i> .	[14] Two different interictal spike patterns anticipate ictal activity in vitro.
[6] Video image-based analysis of single human induced pluripotent stem cell derived cardiomyocyte beating dynamics using digital image correlation.	[15] A Koulouri V, Rimpilainen C.H, Wolters S, Purtilainen A, Rezaei M, Antonakakis M, C. Pliastro Q, He. <i>Conditionally Gaussian Hierarchical Bayesian Inversion of the P20-N20 Component of SEP/SEP measurements with FEM Forward Modeling</i> .
[7] Distinguishing Hidden Markov Chains.	[16] (Brainstorm) EEG and epilepsy.
[8] Video image-based analysis of single human induced pluripotent stem cell derived cardiomyocyte beating dynamics using digital image correlation.	[17] (FieldTrip) Processing and analysis of spike-train data.
[9] Ian Goodfellow, Yoshua Bengio, and Aaron Courville. <i>Estimating the dimension of a model</i> . Annals of Statistics, 2016.	[18] (SPM12) fMRI and some clinical practical data processing.
	[19] <i>Interictal high-frequency oscillations (HFOs) as predictors of high frequency and conventional seizure onset zones</i> .

- | | |
|---|---|
| [1] G E van der Maaten, J.J.P.; Hinton. Visualizing Data Using t-SNE. <i>Journal of Machine Learning Research</i> , 2008. | [10] S Kullback. <i>Information Theory and Statistics</i> . John Wiley Sons, 1978. |
| [2] Louppe/Lévesque de Liège Joeri Hermans, Volodimir Begy Gilles. <i>Likelihood-free MCMC with Amortized Approximate Likelihood Ratios</i> . | [11] <i>On the Importance of Strong Baselines in Bayesian Deep Learning</i> . |
| [3] Annika Ahtianen Qiu He, Jari Hyttinen. Classification of epileptic ictal with Bayes inference Model. <i>Neuroelectronic Interfaces (GRS) Gordon Research Semina</i> , 2019. | [12] RNA single sequences report. |
| [4] Dentate granule and mossy cells exhibit distinct spatiotemporal responses to local change in a one-dimensional landscape of visual tactile cues. | [13] Genetic regulation of gene expression in the epileptic human hippocampus. |
| [5] Lévesque <i>Robustness Guarantees for Bayesian Inference with Gaussian Processes</i> . | [14] Two different interictal spike patterns anticipate ictal activity in vitro. |
| [6] Video image-based analysis of single human induced pluripotent stem cell derived cardiomyocyte beating dynamics using digital image correlation. | [15] A. Koulouri V. Rimpilainen C.H. Wolters S. Pursiainen A. Rezaei, M. Antonakakis M. C. Piasra Q. He. Conditionally Gaussian Hierarchical Bayesian Inversion of the P20-N20 Component of SEP/SEP measurements with FEM Forward Modeling. |
| [7] Distinguishing Hidden Markov Chains. | [16] (Brainstorm) EEG and epilepsy. |
| [8] Video image-based analysis of single human induced pluripotent stem cell derived cardiomyocyte beating dynamics using digital image correlation. | [17] (FieldTrip) Processing and analysis of spike-train data. |
| [9] Ian Goodfellow, Yoshua Bengio, and Aaron Courville. Estimating the dimension of a model. <i>Annals of Statistics</i> , 2016. | [18] (SPM12) fMRI and some clinical practical data processing. |
| | [19] <u>Interictal high-frequency oscillations (HFOs) as predictors of high frequency and conventional seizure onset zones</u> . |